SCIENCE CHINA
Chemistry

•COMMUNICATIONS•

February 2020 Vol.63 No.2: 192–197
https://doi.org/10.1007/s11426-019-9658-1

Cobalt-containing covalent organic frameworks for visible light-driven hydrogen evolution

Jian Wang[1,2], Jian Zhang[1], Shing Bo Peh[1], Guoliang Liu[1], Tanay Kundu[1], Jinqiao Dong[1], Yunpan Ying[1], Yuhong Qian[1] & Dan Zhao[1*]

[1]*Department of Chemical and Biomolecular Engineering, National University of Singapore, Singapore 117585, Singapore;*
[2]*School of Chemistry and Materials Science, Jiangsu Normal University, Xuzhou 221116, China*

Received September 16, 2019; accepted November 25, 2019; published online December 12, 2019

Covalent organic frameworks (COFs) have recently emerged as a new class of photocatalysts. However, integrated design is crucial to maximizing the performance of COF-incorporating photocatalytic systems. Herein, we compare two strategies of installing earth-abundant metal-based catalytic centers into the matrice of a 2D COF named NUS-55. Compared to NUS-55(Co) prepared from the post-synthetic metalation of coordination sites within the COF, the molecular co-catalyst impregnated NUS-55/$[Co(bpy)_3]Cl_2$ achieves a seven-fold improvement in visible light-driven H_2 evolution rate to 2,480 μmol g^{-1} h^{-1}, with an apparent quantum efficiency (AQE) of 1.55% at 450 nm. Our results show that the rational design of molecular anchoring sites in COFs for the introduction of catalytic metal sites can be a viable strategy for the development of highly efficient photocatalysts with enhanced stability and photocatalytic activities.

covalent organic frameworks (COFs), photocatalytic H_2 evolution, non-precious-metal, post-synthetic modification, Co (II)-cooperation

Citation: Wang J, Zhang J, Peh SB, Liu G, Kundu T, Dong J, Ying Y, Qian Y, Zhao D. Cobalt-containing covalent organic frameworks for visible light-driven hydrogen evolution. *Sci China Chem*, 2020, 63: 192–197, https://doi.org/10.1007/s11426-019-9658-1

Because of their unique physicochemical properties, porous organic materials [1–4] have attracted considerable interests in various technological and energy-related applications such as gas storage and separation [5,6], catalysis [7–9], environmental remediation [10,11], etc [12–17]. In the realm of photocatalysis, covalent organic frameworks have been recognized as excellent catalyst materials possessing highly advantageous attributes [18,19], including (1) high structural porosity for the transport of reaction components, (2) extended conjugation for improved charge carrier mobility and longer excited life-times, (3) crystalline long-range order for the facilitation of charge transport and charge separation, (4) chemical stability due to covalent linkages, and (5) high extent of tunability by modifying building blocks at the molecular level. Thus, these imply the potential of COFs to become avant-garde in photocatalytic research.

Nowadays, the prospect of clean energy production by generating hydrogen using sunlight is highly attractive [20,21]. Besides maximizing the catalytic efficiency, the ongoing development also seeks to minimize the usage of platinum co-catalyst in favor of cheaper, earth-abundant alternatives such as cobalt, nickel, copper, etc [22,23]. To date, several COF-based systems have been developed for this purpose. Systems involving Pt co-catalysts have attained hydrogen evolution rates as high as 1,700 μmol g^{-1} h^{-1} [24], whereas Lotsch and co-authors [25] have reported a noble metal-free system that attains a hydrogen evolution rate of 782 μmol g^{-1} h^{-1}. Several strategies exist for the inclusion of metal coordinating sites which can serve as anchoring points for co-catalysts in the hydrogen evolution reactions (HER).

*Corresponding author (email: chezhao@nus.edu.sg)

For example, imine-linked COFs with appropriate structure may be used to anchor metal ions [26]; monomers such as bipyridine may be used to synthesize COFs with homogeneous distribution of chelating sites [27,28]. Alternatively, molecular catalysts may be included by leveraging weak supramolecular interactions with the COF matrix [25]. However, to our knowledge, the discussion and comparison of the relative hydrogen production efficiency of these strategies have yet to be reported. Herein, we report the design and synthesis of a novel COF named NUS-55, which is enriched with potential coordination sites. NUS-55 is used as a scaffold to afford two cobalt-comprising materials. Specifically, the cobalt (II)-chelating COF [NUS-55(Co)] was obtained by post-synthetic modification; whereas the NUS-55/$[Co(bpy)_3]Cl_2$ was prepared by confining the molecular co-catalyst using weak interactions. We for the first time performed the comparison of the relative hydrogen production efficiency between these two strategies, demonstrating that the rational design of molecular anchoring sites in COFs can be a viable strategy for the development of highly stable and efficient photocatalysts.

NUS-55 $\{C_{18}H_{12}N_6O_4\}_n$ was synthesized by condensation of [2,2′-bipyridine]-5,5′-dicarbohydrazide (BPDC) with 1,3,5-triformylphloroglucinol (TFP) under solvothermal conditions (Figure 1(a)). The powder X-ray diffraction (PXRD) patterns of NUS-55 indicate an intense peak at 2θ=2.62° corresponding to the (100) reflection, with minor peaks at 4.64° and 26.2° that can be attributed to (2-10) and (001) reflections, respectively (Figure 1(b)). According to the previous studies [27,28], a structural model of *cis* conformation of bipyridine moiety in NUS-55 was constructed with an AA eclipsed layer stacking, affording a calculated PXRD pattern which is consistent with the observed reflections; while the staggered AB mode produced a profile that deviates from the experimental pattern (Figure S1, Supporting Information online). Hence, we propose the hexagonal space group P_{-6} for NUS-55. Pawley refinement of the experimental NUS-55 pattern yielded unit cell parameters of a=b=38.6 Å, c=3.4 Å, α=β=90°, and γ=120° (Table S1, Supporting Information online). The π-π stacking distance between adjacent COF layers was calculated to be 3.4 Å from the d spacing between (001) planes. NUS-55 exhibits hexagonal 1D channels with a channel size of ca. 2.9 nm measured through crystal models.

The successful condensation reactions are supported by Fourier transform infrared spectroscopy (FTIR, Figure S2), showing the disappearance of the N−H stretching bands of BPDC (3,100–3,300 cm^{-1}) and the carbonyl stretching bands of TFP (1,633 cm^{-1}), together with the appearance of new stretching bands at 1,625, 1,590, and 1,272 cm^{-1} due to the formation of new C=O, C=C, and C–N bonds. The solid-state ^{13}C cross-polarization magic-angle spinning nuclear magnetic resonance (CP/MAS NMR) spectroscopy reveals

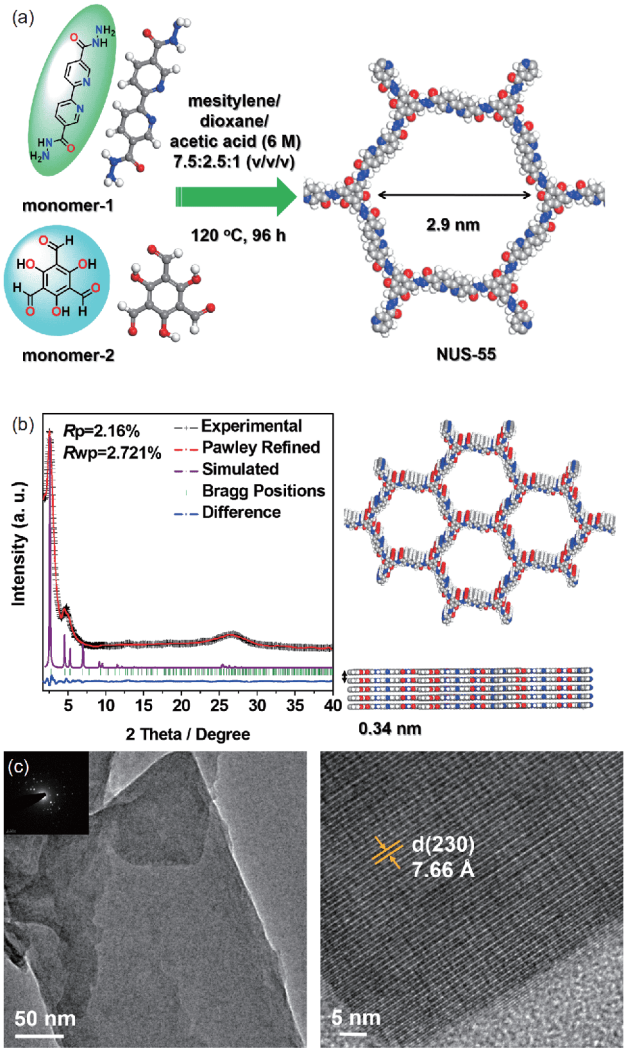

Figure 1 (a) Synthetic scheme of NUS-55; (b) powder X-ray diffraction (PXRD) patterns of NUS-55, with the simulated crystal structure of NUS-55 shown on the right; (c) left: TEM images of NUS-55 (inset: the corresponding selected-area electron diffraction (SAED) patterns). Right: HR-TEM images of NUS-55 (color online).

the presence of keto-form carbonyl carbon at 207 ppm, further confirming the proposed chemical structure of NUS-55 (Figure S3). Compared to BPDC and TFP, the solid-state UV-Vis spectrum (Figure S4) of NUS-55 exhibits a new broad band at 485 nm due to π-electron delocalization in NUS-55 [29]. The activated NUS-55 possesses high thermal stability of up to 300 °C based on the thermogravimetric analysis (Figure S5). Scanning electron microscopy (SEM) shows that NUS-55 crystallizes with a rod-like morphology (Figure S6). The selected-area electron diffraction (SAED) pattern of NUS-55 (inset of Figure 1(c) left) reveals the highly ordered crystallographic plane, and crystal lattices can still be identified in the HR-TEM images of NUS-55 (Figure 1(c) right), further indicating the presence of crystalline order in small domains. The permanent porosity of NUS-55 was evaluated by N_2 sorption experiments at 77 K (Figure 2

(c)). The calculated Brunauer-Emmett-Teller (BET) surface area is 340 $m^2 g^{-1}$. The pore size distribution of NUS-55 indicates a maximum at 2.7 nm, agreeing well with the crystal models (Figure S7).

Following the successful synthesis of NUS-55, the cobalt-modified NUS-55 (NUS-55(Co)) was prepared, and the PXRD pattern of NUS-55(Co) indicates its isoreticular nature with the pristine NUS-55 (Figure S8). The absence of extra PXRD peaks confirms the absence of any undesired moieties (viz., starting metal precursor, metallic cobalt, or Co-oxide residues) in NUS-55(Co). The FTIR spectrum of NUS-55(Co) shows retention of chemical functionalities present in the pristine NUS-55, except for the red shifting and broadening of the $\nu_{C=O}$ peak, indicating the presence of Co–O coordination in the NUS-55(Co) framework (Figure 2 (b)) [30]. The solid-state UV-Vis spectrum of NUS-55(Co) shows a new intense absorption band at 540 nm, corresponding to the charge transfer transition (Figure S9).

The X-ray photoelectron spectroscopy (XPS) data of NUS-55 indicate the presence of only nitrogen, oxygen, and carbon. Upon cobalt impregnation, two broad sets of signals corresponding to $2p_{3/2}$ (780.5 eV) and $2p_{1/2}$ (795.8 eV) core levels of cobalt were observed, evidencing the successful metallation (Figure S10). The N 1s spectra indicate a shift in binding energy corresponding to that of secondary nitrogen (from 400.53 to 400.06 eV), whereas the peak position of pyridinic nitrogen (399.15 eV) remains unchanged, suggesting the complexation of cobalt to the COF by the tridentate chelating groups (ONO) instead of its bipyridinic units (Figure 2(d)). The ^{13}C CP/MAS NMR spectrum of NUS-55(Co) shows a significant upfield shift (7 ppm) of the carbonyl (–C=O) carbon compared to that of NUS-55 (207 ppm), further confirming the XPS results (Figure S3). The N_2 isotherm evaluation of NUS-55(Co) indicates a 31% loss in BET surface area. Thermogravimetric analysis of NUS-55(Co) in air reveals a cobalt content of ca. 9 wt% in the framework, matching well with the inductively coupled plasma (ICP) analysis result (9.36 wt% cobalt content). No distinct changes in morphology were observed in NUS-55(Co) compared to that of the pristine NUS-55. Moreover, the TEM images do not show the presence of any metal nanoparticles or metal oxide particles in the COF matrix of NUS-55(Co). Finally, the EDX elemental mapping reveals a uniform distribution of the Co and N contents in NUS-55(Co) (Figure 2 (e)). All the above results demonstrate the successful formation of NUS-55(Co), where the complexation of cobalt to the COF is realized through the tridentate chelating groups (ONO).

The intensity of luminescence spectrum of NUS-55(Co) is weaker than that of NUS-55, indicating that there is electron transfer from NUS-55 to cobalt(II) centers (Figure S11). Photocatalytic experiments were performed to determine the H_2 production performance of NUS-55(Co). A maximum H_2

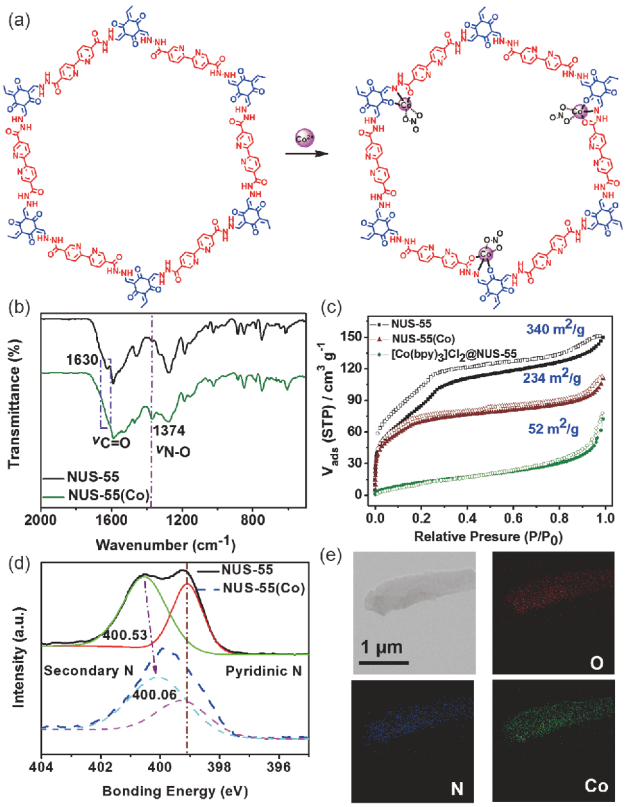

Figure 2 (a) Schematic representation of the synthesis of NUS-55(Co) via Co(II) impregnation. (b) Comparison of the FTIR spectra of NUS-55 and NUS-55(Co). (c) N_2 sorption isotherms of NUS-55 before and after Co-treatments, and NUS-55 after adsorbing $[Co(bpy)_3]Cl_2$ (filled, adsorption; open, desorption). (d) Deconvoluted XPS N 1s spectra of NUS-55 and cobalt-impregnated NUS-55(Co). (e) TEM and energy dispersive X-ray (EDX) elemental mapping images of NUS-55(Co) (color online).

production rate of 433 μmol g^{-1} h^{-1} (Figure 3(c)) was attained after optimizing the quantity of triethylamine (TEA), pH values, and Co(II)-loading amounts of the reaction mixture (Figures S12, S13 and Table S3), corresponding to an apparent quantum efficiency (AQE) of 0.37% at 450 nm. Control experiments confirmed zero H_2 production when any individual component of the photocatalytic system was absent. Despite the promising performance, a repeat run using the recovered NUS-55(Co) catalyst and fresh solution indicated a 48% loss in hydrogen production rate. ICP-MS analysis of the supernatant revealed 42.8% of cobalt in NUS-55(Co) leaching into solution during the catalytic experiment, suggesting that the reduction in active Co(II) centers in NUS-55(Co) is the primary cause for the deterioration in performance. Meanwhile, PXRD pattern of the recovered NUS-55(Co) evidenced the retention of crystallinity, confirming the stability of the parental NUS-55 framework.

Our next effort is to increase the stability of the catalyst. Because of the noncovalent linkage by relatively weak and dynamic interactions, supramolecular materials have the reversibility and can be easily recycled [31]. Thus, the supramolecular weak interaction approach between NUS-55

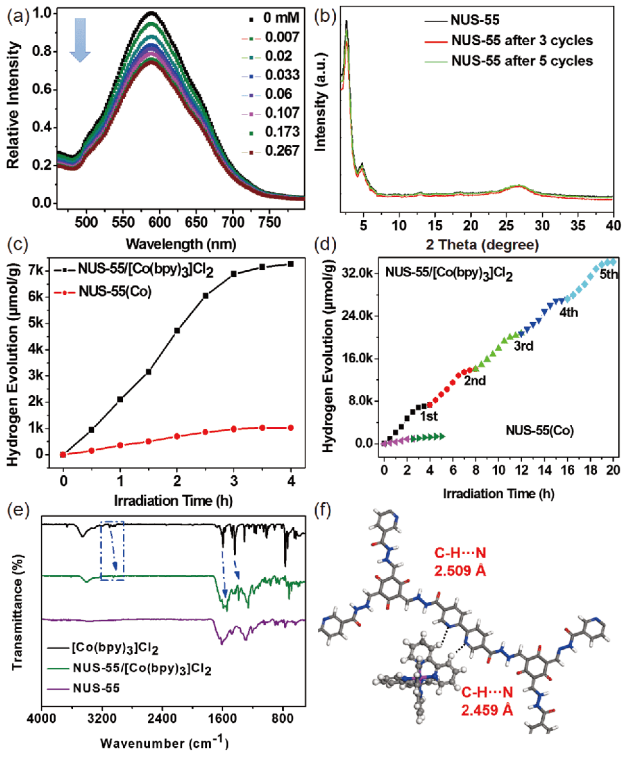

Figure 3 (a) Emission spectra of NUS-55 (2.65 μM) suspension in 1:1 EtOH/H_2O upon addition of $[Co(bpy)_3]Cl_2$. (b) PXRD patterns of NUS-55 before and after 3 and 5 cycles of catalytic reactions. (c) Comparison of H_2 generation between NUS-55(Co) and NUS-55 suspension containing 8.4 μM of $[Co(bpy)_3]Cl_2$. (d) Time dependence of H_2 production of the system with NUS-55(Co) upon adding a fresh solution of TEA (5%, *v*/*v*) every 2.5 h or NUS-55/$[Co(bpy)_3]Cl_2$ upon adding a fresh solution of $[Co(bpy)_3]Cl_2$ (8.4 μM) and TEA (5%, *v*/*v*) every 4 h, respectively. (e) FTIR spectra of $[Co(bpy)_3]Cl_2$ (top), NUS-55 obtained after the absorption of $[Co(bpy)_3]Cl_2$ (middle), and pure NUS-55 (bottom). (f) Scheme of the interaction between NUS-55 and $[Co(bpy)_3]Cl_2$ computed using density functional theory (DFT) calculations (color online).

and cobalt(II)-based proton reduction catalyst ($[Co(bpy)_3]Cl_2$, a commonly used proton reduction catalyst) [32] was developed. The addition of 0.267 mM of $[Co(bpy)_3]Cl_2$ to 0.1 mM of NUS-55 suspension quenched 27% of the emission intensity of NUS-55 with the Stern-Volmer constant K_{SV}=5.9±0.12×10^3 M^{-1} (Figures 3(a) and S14). In addition, transient emission spectra of NUS-55 suspension showed that their fluorescence lifetime decreased from 1.08 to 0.64 ns in the presence of $[Co(bpy)_3]Cl_2$ (Figure S15). This quenching behaviour can be assigned to the photoinduced electron transfer process from the excited state of NUS-55 to $[Co(bpy)_3]Cl_2$. Solid-state electrochemical measurement results suggest a reversible redox wave at $E_{1/2}$=0.28 V, assignable to the redox potential of the NUS-55$^+$/NUS-55 couple (Figure S17). The redox potential of the excited state NUS-55$^+$/NUS-55* couple was calculated as −2.02 V on the basis of a free energy change (E^{0-0}=2.3 eV) between the ground state and the vibrationally related excited state (Figure S16). This potential was more negative than that of $[Co(bpy)_3]Cl_2$ (E^0=–0.74 V), suggesting that reduction of the Co(II)-center by the photo-excited NUS-55 is thermodynamically feasible. In addition, from the optical bandgap (E_g=1.39 eV) determined from the UV-Vis diffuse reflectance (DR) spectrum (Figure S18), the valence band (VB) and conduction band (CB) edges of NUS-55 can be estimated to be E_{CB}=−4.98 eV and E_{VB}=−6.37 eV, following the equations E_{CB}=−($E_{1/2}$+4.7) eV and E_{VB}=E_{CB}–E_g [33]. Based on a comparison of these values with the reduction onset potential of the $[Co(bpy)_3]Cl_2$ molecular catalyst system (E^0=–0.74 V), it is likely that NUS-55 can transfer electrons to the $[Co(bpy)_3]Cl_2$ co-catalyst system; therefore, it is possible for the proton reduction in the NUS-55/$[Co(bpy)_3]Cl_2$ system to realize photocatalytic H_2 generation.

The photocatalyzed HER using 2 mg of NUS-55 and different amounts of $[Co(bpy)_3]Cl_2$ suspension under the same condition (pH=10) was carried out (Figure S19). $[Co(bpy)_3]Cl_2$ with a concentration of 8.4 μM resulted in a H_2 production rate of 2,480 μmol g^{-1} h^{-1} in the first 2 h, which is comparative with the previously reported azine-based COFs (1,703 μmol g^{-1} h^{-1}) [24] and hydrazone-based COFs (1,970 μmol g^{-1} h^{-1}) [34]. The peak hydrogen production is 7,256 μmol g^{-1} following 4 h of irradiation, corresponding to a TON of 17.4 based on $[Co(bpy)_3]Cl_2$ (Figure 3(c, d)), and is approximately 7-times higher than that of NUS-55(Co). To quantify the spectral distribution of the photocatalytic activity of NUS-55/$[Co(bpy)_3]Cl_2$ system, the AQE was calculated using four different band-pass filters with central wavelengths at 450, 500, 550, and 600 nm, respectively. These measurements clearly indicate that NUS-55 shows an AQE profile that closely tracks the UV-Vis absorption spectrum, and the best AQE is 1.55% with a 450 nm band-pass filter (Figure S20). This value is comparable to that of the previously reported COF-based catalysts in photocatalytic H_2 production (Table S4). Furthermore, control experiments with the absence of any of these individual components including NUS-55, $[Co(bpy)_3]Cl_2$, and TEA all led to failure in producing hydrogen under the same experimental conditions, thus demonstrating that all three species are essential for hydrogen generation. Recycling experiments on $[Co(bpy)_3]Cl_2$/NUS-55 were also performed. In total, 34,180 μmol g^{-1} of H_2 was obtained after 5 cycles of catalysis (20 h). The unchanged PXRD pattern of NUS-55 after the catalytic experiments confirms its high stability (Figure 3(b)), which is further confirmed by the TEM image (Figure S21). Notably, NUS-55 still remains porous after the catalytic experiments (Figure S22).

The high efficiency and stability of NUS-55/$[Co(bpy)_3]Cl_2$ system inspired us to further investigate the potential factors influencing the photoinduced hydrogen evolution process. Characteristic peaks of free $[Co(bpy)_3]Cl_2$ in the FTIR spectra at 3,104, 1,596, and 1,443 cm^{-1}, corresponding respectively to C–H, C=C, and C=N stretching vibrations,

experienced red-shifts to 3,060, 1,557, and 1,392 cm^{-1}, respectively, upon inclusion within the NUS-55 framework (Figure 3(e)). In addition, thermogravimetric analysis of NUS-55 after adsorbing $[Co(bpy)_3]Cl_2$ was also carried out, revealing more metal oxides left compared to that of the original NUS-55 (Figure S23). All the related data suggest the existence of weak interactions and adsorption between the molecular co-catalyst and the COF. Meanwhile, the reduction of BET surface area of the COF to 52 $m^2 g^{-1}$ after treatment with $[Co(bpy)_3]Cl_2$ implies that most of the porous channels of NUS-55 are occupied by $[Co(bpy)_3]Cl_2$ upon complexing. Density functional theory (DFT) calculations were performed to elucidate the interactions between NUS-55 and $[Co(bpy)_3]Cl_2$. As shown in Figure 3(f), C–H···N interactions are possible between $[Co(bpy)_3]Cl_2$ and the BPDC units in the COF, corresponding to the shortest distances of 2.459 and 2.509 Å, respectively. The calculations support the existence of weak supramolecular interactions between NUS-55 and $[Co(bpy)_3]Cl_2$, which may play an important role in encouraging the efficient photoinduced electron transfer process, further improving the efficiency of H_2 evolution. Thus, NUS-55/$[Co(bpy)_3]Cl_2$ system shows significantly improved performance compared to that of NUS-55(Co) system, with the possible reason that the immobilized Co-centers in NUS-55(Co) can potentially engage in photocatalysis with direct electron transfer (ET) from NUS-55, whereas the energy transfer (ET) from NUS-55 to $[Co(bpy)_3]Cl_2$ molecules would likely be slower through this supramolecular interactions. This means that recombination could be a limiting factor in the NUS-55(Co) system, which reduces the H_2 evolution rate. To confirm this result, photocurrent measurements were carried out to unveil the electron-hole (e-h) separation efficiency [35,36]. As expected, NUS-55/$[Co(bpy)_3]Cl_2$ produces a higher photocurrent response than that of NUS-55(Co), reflecting that photo-induced electron-hole (e-h) pairs can be separated more efficiently in NUS-55/$[Co(bpy)_3]Cl_2$ (Figure S24).

In conclusion, a highly porous COF named NUS-55 enriched with coordination sites has been successfully synthesized. The post-synthetic modification of NUS-55 with Co(II) affords NUS-55(Co) as a photocatalyst that can catalyze visible light-driven H_2 evolution reaction with a H_2 evolution rate of 433 μmol $g^{-1} h^{-1}$. In order to further increase the stability and H_2 evolution efficiency of this system, a Co(II)-cooperation supramolecular NUS-55/$[Co(bpy)_3]Cl_2$ system was developed, exhibiting a H_2 evolution rate approximately 7-times higher than that of the NUS-55 (Co) system. Importantly, the Co(II)-coorperating supramolecular system also exhibits a high stability, further indicating the broad prospects of this catalytic system for practical catalytic applications.

Acknowledgements This work was supported by the National Research Foundation of Singapore (NRF2018-NRF-ANR007 POCEMON), the Ministry of Education-Singapore (MOE AcRF Tier 1 R-279-000-540-114, Tier 2 MOE2018-T2-2-148), the Agency for Science, Technology and Research (IRG A1783c0015, IAF-PP A1789a0024), and the Jiangsu Overseas Visiting Scholar Program for University Prominent Young & Middle-Aged Teachers and Presidents.

Conflict of interest The authors declare that they have no conflict of interest.

Supporting information The supporting information is available online at http://chem.scichina.com and http://link.springer.com/journal/11426. The supporting materials are published as submitted, without typesetting or editing. The responsibility for scientific accuracy and content remains entirely with the authors.

1 Côté AP, Benin AI, Ockwig NW, O'Keeffe M, Matzger AJ, Yaghi OM. *Science*, 2005, 310: 1166–1170
2 Cooper AI. *Adv Mater*, 2009, 21: 1291–1295
3 Jin E, Asada M, Xu Q, Dalapati S, Addicoat MA, Brady MA, Xu H, Nakamura T, Heine T, Chen Q, Jiang D. *Science*, 2017, 357: 673–676
4 Ma T, Kapustin EA, Yin SX, Liang L, Zhou Z, Niu J, Li LH, Wang Y, Su J, Li J, Wang X, Wang WD, Wang W, Sun J, Yaghi OM. *Science*, 2018, 361: 48–52
5 Furukawa H, Yaghi OM. *J Am Chem Soc*, 2009, 131: 8875–8883
6 Huang N, Chen X, Krishna R, Jiang D. *Angew Chem Int Ed*, 2015, 54: 2986–2990
7 Banerjee T, Gottschling K, Savasci G, Ochsenfeld C, Lotsch BV. *ACS Energy Lett*, 2018, 3: 400–409
8 Lu M, Li Q, Liu J, Zhang FM, Zhang L, Wang JL, Kang ZH, Lan YQ. *Appl Catal B-Environ*, 2019, 254: 624–633
9 Wang X, Han X, Zhang J, Wu X, Liu Y, Cui Y. *J Am Chem Soc*, 2016, 138: 12332–12335
10 Sun Q, Aguila B, Perman J, Ivanov AS, Bryantsev VS, Earl LD, Abney CW, Wojtas L, Ma S. *Nat Commun*, 2018, 9: 1644
11 Ding SY, Dong M, Wang YW, Chen YT, Wang HZ, Su CY, Wang W. *J Am Chem Soc*, 2016, 138: 3031–3037
12 Lin G, Ding H, Yuan D, Wang B, Wang C. *J Am Chem Soc*, 2016, 138: 3302–3305
13 Chandra S, Kundu T, Kandambeth S, Babarao R, Marathe Y, Kunjir SM, Banerjee R. *J Am Chem Soc*, 2014, 136: 6570–6573
14 DeBlase CR, Silberstein KE, Truong TT, Abruña HD, Dichtel WR. *J Am Chem Soc*, 2013, 135: 16821–16824
15 Cai P, Peng X, Huang J, Jia J, Hu X, Wen Z. *Sci China Chem*, 2019, 62: 385–392
16 Vyas VS, Vishwakarma M, Moudrakovski I, Haase F, Savasci G, Ochsenfeld C, Spatz JP, Lotsch BV. *Adv Mater*, 2016, 28: 8749–8754
17 Zhang K, Guo W, Liang Z, Zou R. *Sci China Chem*, 2019, 62: 417–429
18 Diercks CS, Yaghi OM. *Science*, 2017, 355: eaal1585
19 Huang N, Wang P, Jiang D. *Nat Rev Mater*, 2016, 1: 16068
20 Zhang T, Lin W. *Chem Soc Rev*, 2014, 43: 5982–5993
21 Wang S, Wang X. *Small*, 2015, 11: 3097–3112
22 Eckenhoff WT. *Coord Chem Rev*, 2018, 373: 295–316
23 Artero V, Chavarot-Kerlidou M, Fontecave M. *Angew Chem Int Ed*, 2011, 50: 7238–7266
24 Vyas VS, Haase F, Stegbauer L, Savasci G, Podjaski F, Ochsenfeld C, Lotsch BV. *Nat Commun*, 2015, 6: 8508
25 Banerjee T, Haase F, Savasci G, Gottschling K, Ochsenfeld C, Lotsch BV. *J Am Chem Soc*, 2017, 139: 16228–16234
26 Romero J, Rodriguez-San-Miguel D, Ribera A, Mas-Ballesté R, Otero TF, Manet I, Licio F, Abellán G, Zamora F, Coronado E. *J Mater Chem A*, 2017, 5: 4343–4351
27 Shinde DB, Aiyappa HB, Bhadra M, Biswal BP, Wadge P, Kandambeth S, Garai B, Kundu T, Kurungot S, Banerjee R. *J Mater Chem*

A, 2016, 4: 2682–2690
28 Sun Q, Aguila B, Perman J, Nguyen N, Ma S. *J Am Chem Soc*, 2016, 138: 15790–15796
29 Aiyappa HB, Thote J, Shinde DB, Banerjee R, Kurungot S. *Chem Mater*, 2016, 28: 4375–4379
30 Bhadra M, Sasmal HS, Basu A, Midya SP, Kandambeth S, Pachfule P, Balaraman E, Banerjee R. *ACS Appl Mater Interfaces*, 2017, 9: 13785–13792
31 Ma X, Zhao Y. *Chem Rev*, 2015, 115: 7794–7839
32 Dong J, Wang M, Zhang P, Yang S, Liu J, Li X, Sun L. *J Phys Chem C*, 2011, 115: 15089–15096
33 Cardona CM, Li W, Kaifer AE, Stockdale D, Bazan GC. *Adv Mater*, 2011, 23: 2367–2371
34 Stegbauer L, Schwinghammer K, Lotsch BV. *Chem Sci*, 2014, 5: 2789–2793
35 Zou Z, Ye J, Sayama K, Arakawa H. *Nature*, 2001, 414: 625–627
36 Liu J, Liu Y, Liu N, Han Y, Zhang X, Huang H, Lifshitz Y, Lee ST, Zhong J, Kang Z. *Science*, 2015, 347: 970–974